

EES Catalysis

Accepted Manuscript

This article can be cited before page numbers have been issued, to do this please use: P. Liu, F. Lyu, X. Yang, Z. Zheng, W. Hua, S. Mei, M. Ma, H. Wang, X. Ge, L. Wu, T. Xu, Z. Deng and Y. Peng, *EES Catal.*, 2025, DOI: 10.1039/D5EY00153F.



This is an Accepted Manuscript, which has been through the Royal Society of Chemistry peer review process and has been accepted for publication.

Accepted Manuscripts are published online shortly after acceptance, before technical editing, formatting and proof reading. Using this free service, authors can make their results available to the community, in citable form, before we publish the edited article. We will replace this Accepted Manuscript with the edited and formatted Advance Article as soon as it is available.

You can find more information about Accepted Manuscripts in the [Information for Authors](#).

Please note that technical editing may introduce minor changes to the text and/or graphics, which may alter content. The journal's standard [Terms & Conditions](#) and the [Ethical guidelines](#) still apply. In no event shall the Royal Society of Chemistry be held responsible for any errors or omissions in this Accepted Manuscript or any consequences arising from the use of any information it contains.

Broader context

Electrocatalytic CO₂ reduction (eCO₂R) into valuable chemicals using renewable electricity is a promising strategy to mitigate climate change and achieve carbon neutrality. Its operation in acidic electrolyte is highly desirable due to the alleviated carbon loss, but faces severe challenges, including competing hydrogen evolution reactions (HER), salt precipitation, and water flooding, which collectively undermine the current efficiency and long-term stability. This work, by introducing an innovative asymmetric porous bipolar membrane (BPM) architecture through the integration of electrospun anion-exchange nanofibers (AENFs) with a planar cation-exchange membrane (CEM), addresses critical challenges in eCO₂R under acidic conditions, offering a novel approach to enhance the efficiency, stability, and scalability of membrane electrode assemblies (MEAs) for industrial CO₂ utilization. The optimized BPM configuration demonstrates exceptional performance, achieving stable operation for 325 hours in acidic conditions with an average CO Faradaic efficiency of 88% and a remarkable single-pass CO₂ conversion efficiency of 67% at 300 mA cm⁻² under 15 sccm CO₂ flow. Furthermore, a 25 cm² scale-up MEA is demonstrated, maintaining stable operation over 110 hours with an energy efficiency of 34.2%, outperforming previous benchmarks. This breakthrough has the potential to significantly reduce carbon emissions and combat climate change.



Biphasic Anion-Exchange Nanofibers Enable Bipolar Junction Engineering for Enhanced Electrocatalytic CO₂ Conversion in Acidic Media

New Article Online
DOI: 10.1039/D5EY00153F

Peng Liu,^{†a} Fenglei Lyu,^{†ab} Xiya Yang,^a Zhangyi Zheng,^a Wei Hua,^a Shiwei Mei,^a Mutian Ma,^a Haojun Wang,^a Xiaolin Ge,^c Liang Wu,^c Tongwen Xu,^c Zhao Deng,^{ab} and Yang Peng^{*ab}

^aSoochow Institute for Energy and Material Innovations, College of Energy, Soochow University, Suzhou 215006, China.

^bJiangsu Key Laboratory for Advanced Negative Carbon Technologies, Soochow University, Suzhou 215123, China.

^cState Key Laboratory of Precision and Intelligent Chemistry, School of Chemistry and Materials Science, University of Science and Technology of China, Hefei, Anhui 230026, China.

† These authors contributed equally to this work.

E-mail: ypeng@suda.edu.cn

Abstract

Driven by renewable energies, electrocatalytic CO₂ reduction (eCO₂R) in acidic media using membrane electrode assemblies (MEAs) has emerged as a highly promising approach for large-scale CO₂ utilization with economic viability. Nevertheless, the practical implementation faces significant challenges, including competing hydrogen evolution reaction, salt precipitation, and water flooding, which collectively undermine the long-term Faradaic efficiency and operational durability. In this work, we develop an innovative asymmetric porous bipolar membrane (BPM) architecture by integrating electrospun anion-exchange nanofibers with a planar cation-exchange membrane, and configure it in the forward-bias mode (*f*-BPM) within MEAs to enable efficient acidic eCO₂R. The biphasic anion-exchange nanofibers, comprising polycationic piperidinium copolymer and hydrophobic polyvinylidene difluoride, are engineered to simultaneously optimize ion conductivity, membrane swelling, and mechanical integrity, thereby effectively regulating cation migration, electrochemical impedance, as well as water and gas transport properties. The optimized *f*-BPM configuration demonstrates exceptional performance, maintaining stable operation for 325 hours in acidic conditions while achieving an average CO Faradaic efficiency of 88% and a remarkable single-



pass CO₂ conversion efficiency of 67% at a current density of 300 mA/cm² with a CO₂ flow rate of 15 sccm. Furthermore, the scalability of this technology is successfully demonstrated through the fabrication of a larger 5 × 5 cm² *f*-BPM, showcasing a stable operation over 110 hours with an energy efficiency of 34.2%. This breakthrough represents a significant advancement in acidic MEA technology, marking a crucial step toward industrial-scale implementation of eCO₂R.

View Article Online
DOI: 10.1039/D5EY00153F

Keywords

electrocatalytic CO₂ reduction, membrane electrode assembly, acidic electrolyte, anion-exchange nanofibers, bipolar membrane

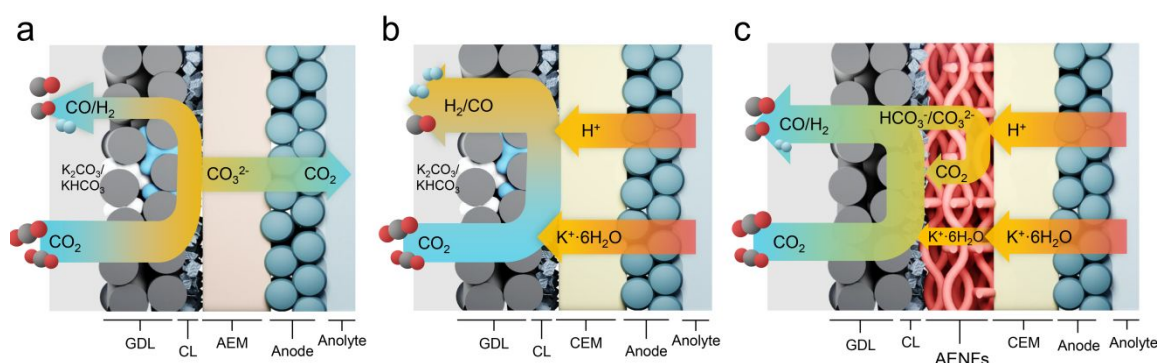
Introduction

Electrocatalytic CO₂ reduction (eCO₂R) powered by renewable electricity represents one of the most promising technologies today to resourcefully recycle anthropogenic CO₂.¹⁻³ Concerning the kinetic energy penalty, two-electron reduction products such as carbon monoxide (CO) and formic acid (HCOOH) are more likely to realize a profitable production in the foreseeable future based on recent techno-economic assessments.⁴⁻⁶ With regard to the electrolyzer design, zero-gap membrane electrode assemblies (MEAs) operated under alkaline/neutral conditions are state-of-the-art, owing to the improved CO₂ mass transport, reduced ohmic losses, and favored chemical environment (**Scheme 1a**).^{3, 7-9} However, the use of anion-exchange membranes (AEMs) in these systems introduces significant challenges. AEMs facilitate the transport of large (bi)carbonate ions formed by the reaction of CO₂ with hydroxyl anions, leading to CO₂ crossover and increased ion migration resistance.^{10, 11} Moreover, the alkali cations would inevitably migrate to the cathode through co-ion leakage, precipitated as (bi)carbonate salts to restrain CO₂ transport on the gas diffusion electrode (GDE). This would further exacerbate disastrous issues such as hydrogen evolution reaction (HER) and water flooding.¹² Thus, before the AEM-based MEA can be practically deployed, issues of CO₂ crossover and salt precipitation must be addressed for extended efficiency and stability.

eCO₂R under acidic condition using cation exchange membranes (CEMs) can effectively sidestep the above issues of CO₂ crossover (**Scheme 1b**).^{3, 13-16} The migration of anions from cathode to anode can be mostly blocked by the fixed anionic groups in CEM via Donnan exclusion.¹⁷ The formation of (bi)carbonate salts in the gas diffusion layer of the cathode can be alleviated by reacting with hydroniums migrated from the anolyte.^{18, 19} Nevertheless, the high proton concentration at the cathode surface often leads to HER dominance, significantly



reducing the Faradaic efficiency (FE) of $e\text{CO}_2\text{R}$.²⁰ To counteract this, alkali cations from the anolyte or cationic ionomers coated on the cathode surface are employed to create an electrostatic barrier, limiting excessive proton flux.^{19, 21-24} This, over time, would eventually



cause salt precipitation and water flooding due to the rising local pH at the cathode surface as protons are consumed. Furthermore, reports on acidic MEAs with larger electrode areas (e.g., $>5\text{ cm}^2$) remain scarce, highlighting a critical gap in scaling up this technology.

Scheme 1. Electrocatalytic CO_2 reduction ($e\text{CO}_2\text{R}$) in zero-gap membrane electrode assemblies (MEAs). (a) alkaline/neutral condition with AEM, (b) acidic condition with CEM, (c) acidic condition with the bipolar AENFs/CEM proposed in this study.

As an alternate solution to neutral/alkaline and acidic $e\text{CO}_2\text{R}$ systems, bipolar membranes operated in forward bias (abbreviated here as $f\text{-BPM}$) have been explored to configure zero-gap MEAs, even enabling the use of pure water as the anolyte.²⁵ In a typical $f\text{-BPM}$ setup, the AEM facing the cathode creates an alkaline environment conducive to selective CO_2 reduction, while the CEM facing the anode facilitates proton transport and blocks (bi)carbonate anion crossover.^{26, 27} Despite the improved CO_2 utilization, MEAs operated under the $f\text{-BPM}$ mode face challenges of high cell voltage due to the large internal resistance, mechanical instability at the bipolar junction caused by mismatched CEM/AEM swelling rates, and stress accumulation from trapped CO_2 and H_2O .²⁸ To address these issues, researchers have contrived various tactics, including perforating the AEM to recirculate CO_2 and H_2O stalled in the junction,²⁹ direct membrane deposition via automated spray coating of AEM/CEM ionomers,³⁰ asymmetric BPM with differential AEM/CEM thickness,³¹ and imprinting microfluidic channels into the bipolar junction.³² While these efforts have advanced the field, most $f\text{-BPM}$ s remain limited to short-term operation (tens of hours) and small form factors.

In this study, we address the persistent issues of blistering and delamination in $f\text{-BPM}$ s²⁸⁻³⁰ by designing a zero-gap MEA with an asymmetric porous bipolar junction. This architecture integrates electrospun fibrous AEMs with a planar CEM, leveraging the interconnected voids and channels within the nanofibers to alleviate mechanical stress caused by swelling mismatch and trapped water and gas. The biphasic nature of the electrospun nanofibers comprising hydrophobic polyvinylidene difluoride (PVDF) and ionic *m*-terphenyl *p*-terphenyl



piperidinium copolymer (MTCP) enables to systemically tailor the ion transport, membrane swelling and mechanical strength. When operated under acidic conditions with alkaline cations, the resulting *f*-BPM not only suppresses cation migration—thereby inhibiting HER and salt precipitation—but also facilitates CO₂ recirculation from the junction to the cathode, enhancing CO₂ utilization and reducing membrane stress (**Scheme 1c**). As a result, MEAs engaging the novel *f*-BPM architecture demonstrated a prolonged eCO₂R operation for 325 hours under acidic conditions with an average CO Faradaic efficiency of 88%. A remarkable CO₂ utilization was attained at 300 mA/cm² showcasing the single pass conversion (SPC) of 67% under 15 sccm of CO₂ flow. What's more, A 25 cm² *f*-BPM achieved stable operation over 110 hours with an energy efficiency of 34.2%, marking a significant step toward industrial feasibility.

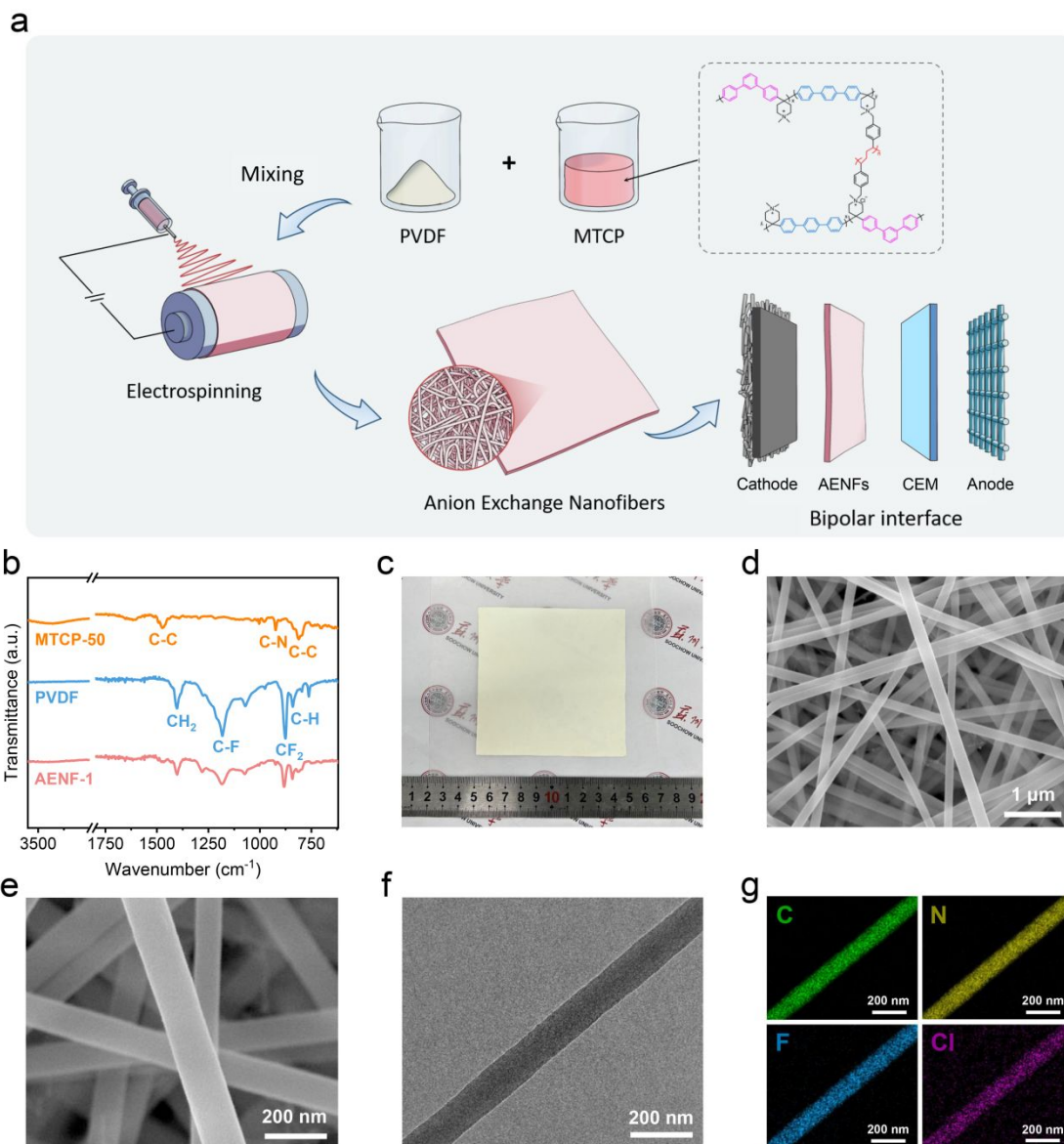
Results

Fibrous membranes composed of the anion exchange ionomer (MTCP-50)³³ reinforced by PVDF were fabricated via the electrospinning method as detailed in the experimental section. The chemical structure of MTCP-50, depicted in **Figure 1a**, consists of a crosslinked copolymer with a 1:1 ratio of *m*-terphenyl and *p*-terphenyl piperidinium. This polymer has been reportedly manifesting high OH⁻ ion conductivity (78.4 mS/cm at 30 °C) and ion exchange capacity (2.53 mmol/g), as well as a superb chemical stability in 1 M KOH for over 8000 hours.³³ By varying the MTCP/PVDF mass ratio (*x*), a series of anion-exchange nanofibers (denoted as AENF-*x*) were synthesized. Infrared (IR) spectrum taken on the exemplary AENF-1 confirmed the co-existence of both PVDF and MTCP-50 in the nanofibers (**Figure 1b**). PVDF not only provides mechanical support, ensuring the durability of the nonwoven structure (**Figure 1c**), but also modulates the hydrophobicity and swelling behavior of the composite, which are critical for regulating water and gas transport. Scanning electron microscopy (SEM) and transmission electron microscopy (TEM) images revealed that the nanofibers exhibit uniform thickness, with an average diameter of approximately 150 nm (**Figure 1d-f**). Elemental mapping further confirmed the homogeneous distribution of carbon (C), nitrogen (N), fluorine (F), and chlorine (Cl) within the nanofibers (**Figure 1g**). The interlaced fibers form tortuous voids and channels of varying sizes, which enhance mass transport properties that can be finely tuned by adjusting the MTCP/PVDF ratio (*x*) and thickness (*y*).

To investigate the impact of membrane thickness, AENF-1 (with a fixed MTCP/PVDF ratio, *x* = 1) was fabricated at three thicknesses: *y* = 15 ± 2, 30 ± 2, and 60 ± 3 μm. Prior to use, all AENFs were sequentially treated with 1 M KOH and deionized (DI) water to activate the membrane. The gas permeability of AENF-1-*y* under wet conditions was evaluated using



differential pressure tests.²⁹ Humidified CO₂ was forced through the wetted membrane in an MEA fixture, and the pressure drop across the membrane was monitored (**Figure S1**). As expected, the gas permeability decreased with increasing membrane thickness, demonstrating a strong correlation between thickness and pressure drop (**Figure S2**). To assess mechanical



strength, tensile tests were performed on wetted AENF-1- y membranes immediately after taking out from DI water (**Figure S3**). The results revealed a monotonic increase in mechanical strength with thickness, ranging from 4.48 MPa ($y = 15 \mu\text{m}$) to 16.67 MPa ($y = 60 \mu\text{m}$) (**Figure S4**).

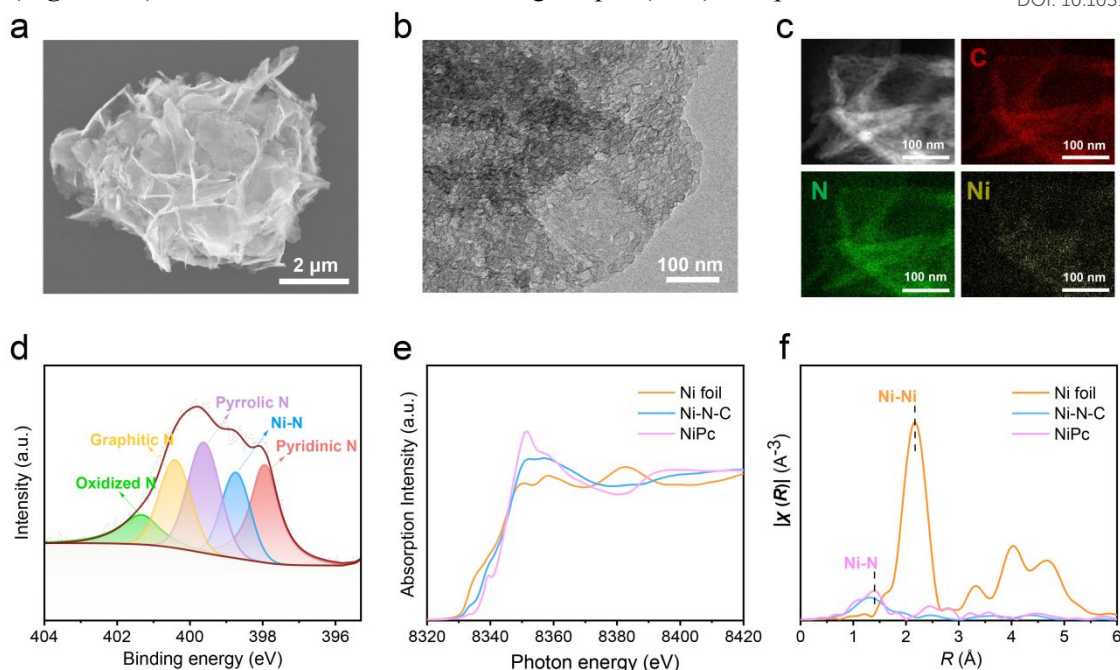
Figure 1. Fabrication and characterization of AENFs. (a) Schematic illustration of the composition and fabrication of AENFs. (b) Infrared spectra of MTCP-50, PVDF and AENF-1. (c) Photograph, (d, e) SEM images of various magnifications, (f) TEM image, and (g) EDX elemental mapping images of AENF-1.

Prior to electrochemical testing, we assembled a membrane electrode assembly (MEA) containing only a Nafion HP and AENF-1- y to assess their ability of suppressing H⁺ migration



(Figure S5).³⁴ AENF-1-60 maintained a higher pH (3.58) compared to thinner AENF-1-15

Open Access Article. Published on 04 June 2025. Downloaded on 6/16/2025 10:58:03 PM.
This article is licensed under a Creative Commons Attribution 3.0 Unported Licence.
DOI: 10.1039/D5EY00153F



(2.87) and CEM-only control sample (2.83) after 30 minutes. The enhanced suppression was attributed to the longer H^+ migration path and more cationic groups in thicker membranes. These findings highlight the critical role of membrane thickness in controlling H^+ crossover.

Figure 2. Morphological and physico-chemical characterizations of the Ni-N-C catalyst. (a) SEM, (b) TEM, (c) HAADF-STEM elemental mapping images, and (d) XPS N 1s spectrum of the Ni-N-C catalyst. (e) XANES and (f) FT-EXAFS spectra of the Ni-N-C catalyst in reference to the Ni foil and nickel phthalocyanine.

To further explore the effect of membrane thickness on eCO_2R performance, AENF-1-y was paired with Nafion-HP to form bipolar junctions in acidic MEAs. The cross-sectional images reveal the laminated structure of carbon fiber paper (CFP), catalyst layer (CL) supported on microporous layer (MPL), the AENFs layer and the CEM, which confirm the intimate contact among GDE/CL/AENF-1/CEM (**Figure S6**). These MEAs were operated in forward-bias mode (f -BPM) using an anolyte of K_2SO_4/H_2SO_4 ($C_{K^+} = 0.05 M$, $pH = 2$) and an IrO_x -loaded titanium felt anode. The choice of K_2SO_4/H_2SO_4 with 0.05 M K^+ and $pH = 2$ was guided by the following considerations: 1) K^+ Concentration Optimization: Systematic measurements of CO_2 reduction selectivity across varying K^+ concentrations (0.01–1 M) revealed that using electrolyte with 0.05 M K^+ achieves a balance between high Faradaic efficiency (**Figure S7**) for target products (>95%) and long-term stability. Lower K^+ concentrations minimize salt precipitation and electrode flooding,³⁵ which are critical for sustained operation, while still providing sufficient K^+ to drive eCO_2R . 2) pH Selection: $pH = 2$ was chosen based on prior computational and experimental studies demonstrating its suitability for acidic eCO_2R .¹⁴ Finite element simulations confirm that bulk-phase $pH = 2$ avoids CO_2 hydrolysis to



bicarbonate/carbonate ions ($\text{CO}_3^{2-}/\text{HCO}_3^-$), thereby mitigating carbon loss via bicarbonate/carbonate formation and crossover. While localized pH near the catalyst surface rises during operation, the acidic bulk electrolyte (pH = 2) ensures rapid re-protonation of carbonate species to CO_2 , maintaining adequate CO_2 availability at the reaction interface.

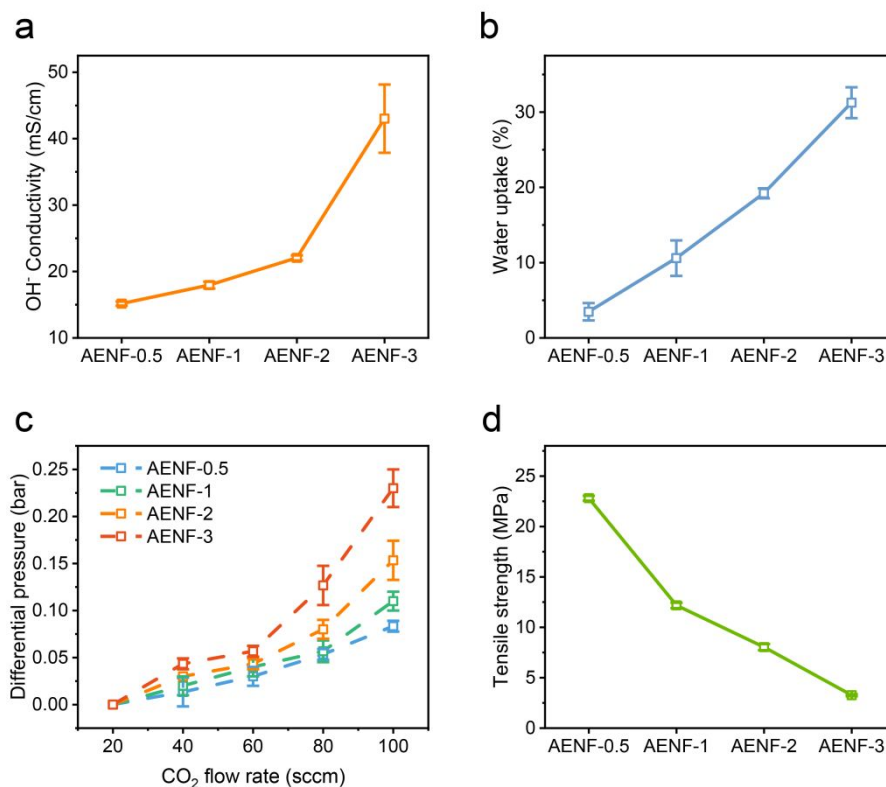
A highly porous Ni-N-C composite was synthesized for using as the cathode catalyst. The synthetic procedure is detailed in the supplementary information. In brief, magnesium carbonate hydroxide served as a structural template, which was coated with a carbonaceous layer via chemical vapor deposition. Following template removal, nickel phthalocyanine (NiPc) molecules were loaded onto the carbon support and thermally annealed to form Ni-N-C complexes. SEM and TEM images revealed that the Ni-N-C composite adopts a nanosheet morphology composed of numerous hollow nanocubes (**Figure 2a, 2b**). High-angle annular dark-field scanning transmission electron microscopy (HAADF-STEM) confirmed the homogeneous distribution of nitrogen (N) and nickel (Ni) elements across the carbon support (**Figure 2c**). X-ray photoelectron spectroscopy (XPS) of the N 1s spectrum indicated that the nitrogen contents are highly heterogeneous, including oxidized, graphitic, pyrrolic, pyridinic, and coordinated Ni-N species. X-ray absorption near-edge structure (XANES) analysis revealed that the valence state of Ni lies between 0 and +2, consistent with single atomic Ni-N-C composites.^{36, 37} Fourier transform-extended X-ray absorption fine structure (FT-EXAFS) further supported this observation, showing no metallic Ni-Ni bonding but a prominent Ni-N peak at 1.4 Å. The high porosity of the carbon support, combined with the uniform dispersion of single-atom Ni sites, endows the Ni-N-C composite with exceptional catalytic activity for CO production in eCO₂R.^{38, 39}

In the eCO₂R tests of *f*-BPM engaging AENF-1 of varying thickness (**Figure S8**), the performance indices and process metrics taken into consideration include: 1) average cell voltage at 100 mA/cm² during a 45-hour galvanostatic operation; 2) average Faradaic efficiency of CO (FE_{CO}); 3) estimated crossover rate of K⁺ from the anolyte; and 4) flooding rate of the cathode. The average flooding and K⁺ crossover rates were estimated by collecting the cathodic effusion and quantifying the K⁺ content via the inductively coupled plasma-atomic emission spectrometry (ICP-OES). While the average cell voltage increased generally with membrane thickness, ranging from 3.45 V for AENF-1-15 to 3.68 V for AENF-1-60, AENF-1-30 exhibited the highest average FE_{CO} of 95% (**Figure S9 and Table S1**). The flooding rate decreased with increasing thickness, while K⁺ crossover reached a minimum at $y = 30$ (**Figure S10**). However, further increasing the thickness to 60 μm led to a rebound in K⁺ crossover, likely due to higher cell voltages exacerbating cation migration.³⁵ These results highlight the effectiveness of the bipolar junction in mitigating K⁺ crossover and water flooding, attributed to the mixed cationic and hydrophobic properties of AENFs. Notably, lower cell voltages are



desirable not only for energy efficiency but also for minimizing K^+ crossover. Based on these findings, AENF-1-30 ($30 \pm 2 \mu\text{m}$) was identified as the optimal thickness, balancing performance and stability. Consequently, in subsequent studies, AENF- x refers to AENF- x -30. The lowest K^+ crossover rate was measured to 1.37 mmol/h in the AENFs system, which was

View Article Online
DOI: 10.1039/D5EY00153F



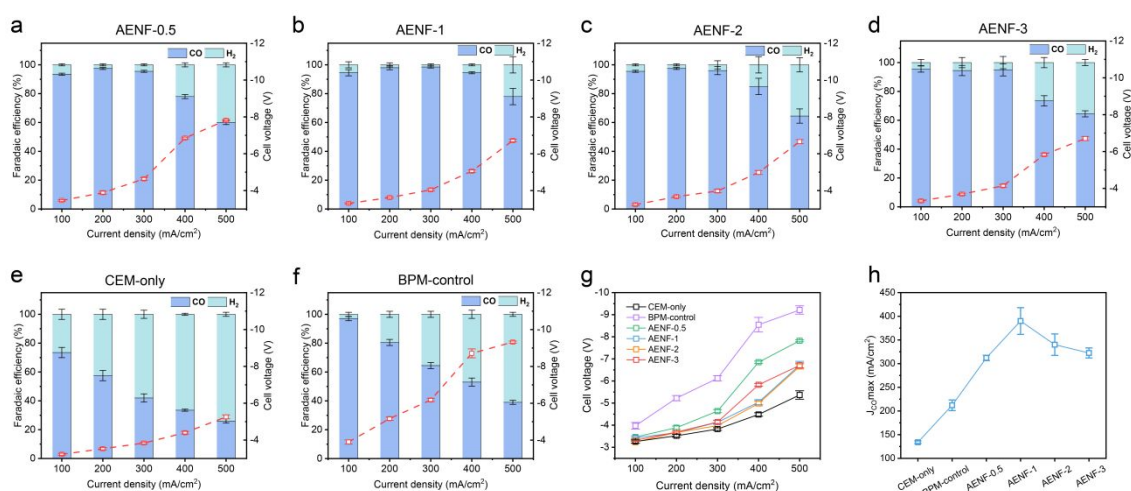
be higher than the values (0.015-0.135 mmol/h) reported in conventional AEM based MEAs (Table S2).^{35, 40, 41} The high K^+ crossover in the AENFs system can be attributed to its porous and loose nanofiber structure, which facilitates faster ion diffusion compared to dense AEMs.

Figure 3. Physico-chemical characterizations of AENF- x . (a) OH⁻ conductivity, (b) water uptake, (c) gas permeability and (d) mechanical strength under the wetted state.

After determining the optimal film thickness (y) using AENF-1, we continue to alter the MTCP/PVDF mass ratio (x) from 0.5 to 1, 2, and 3 to investigate its impact on membrane properties and eCO₂R metrics. SEM images showed that all AENF- x membranes were able to maintain an integral fibrous structure with similar fiber diameters (Figure S11). Infrared (IR) spectra further validated the coexistence of PVDF and MTCP-50 in the nanofibers, with characteristic peak intensities reflecting the changes in MTCP/PVDF ratio (Figure S12). Both water uptake and OH⁻ conductivity measurements indicated that swelling and anion conductivity increased with higher MTCP content (Figure 3a, b and Figure S13). This trend aligns with the well-established relationship between high ion-exchange capacity (IEC) and increased water uptake, which often leads to more pronounced swelling.⁴²⁻⁴⁴ As a result, the gas



permeability of AENF- x decreased with the increasing MTCP/PVDF ratio, with the highest differential pressure observed at $x = 3$ (**Figure 3c**). However, this improvement in ion conductivity came at the cost of mechanical strength. Tensile tests on wetted AENF- x membranes demonstrated a clear decline in mechanical robustness with higher MTCP content, culminating in a tensile strength of just 3.26 MPa for AENF-3 (**Figure 3d**). The poor mechanical strength of AENF-3, coupled with its reduced gas permeability, raises concerns about its long-term stability in f -BPM operations. Accumulated stress from regenerated water and gas within the junction could compromise performance over extended periods. The ability



of suppressing H⁺ migration for AENF- x was also evaluated (**Figure S14**). With the increasing MTCP ratio from 0.5 to 2, improved H⁺ migration suppression ability was observed. But the AENF-3 sample exhibited inferior H⁺ migration suppression compared to other variants, which should be attributed to its higher water uptake (31.25%) which enhanced H⁺ migration.

Figure 4. Faradaic efficiencies of CO (left axis) and the corresponding cell voltages (right axis) at varying current densities recorded from MEAs of various f -BPM configurations: (a) AENF-0.5/Nafion-HP, (b) AENF-1/Nafion-HP, (c) AENF-2/Nafion-HP, (d) AENF-3/Nafion-HP, (e) Nafion-HP alone, and (f) 2D planar BPM composed of the casted MTCP-50 membrane and Nafion-HP. (g) Cell voltages at varying current densities recorded from MEAs of various f -BPM configurations. (h) J_{CO,max} of various f -BPM configurations.

When integrated with Nafion-HP to configure f -BPMs, all AENF- x samples demonstrated high CO selectivity (FE_{CO} > 90%) at current densities below 300 mA/cm² (**Figure 4a-d**). This performance starkly contrasts with that of Nafion-HP alone as the CEM, which exhibited an initial FE_{CO} of <75% at 100 mA/cm², followed by a continuous decline as the current density increased (**Figure 4e**). Apparently, the anion-exchange nanofibers can effectively restrict H⁺ migration and thereby mitigate HER on the cathode. The performances of AENF- x were also much better than that of the control BPM case, in which MTCP-50 was casted into a planar film of 35 ± 3 μ m (**Table S3**) and pressed onto Nafion-HP (**Figure 4f**). Such a 2D planar



junction showed a high initial FE_{CO} of 98% at 100 mA/cm², but quickly deteriorated to less than 40% at 500 mA/cm². In addition, the cell voltages of the control BPM across all current densities were significantly higher than those observed from other cases (**Figure 4g**). Comparing with AENF-1 as an example, at 100 mA/cm², the voltage of AENF-1 (3.51 V) was 0.46 V lower than that of BPM-control (3.97 V).

Experimental investigation using commercial anion-exchange ionomer (Sustainion® XA-9) to replace Nafion ionomer in the cathode catalyst layer with and without the AENF-1 layer was also conducted (**Figure S15**). The FE_{CO} is only ~60% at 100 mA/cm² and decreases to less than 35% with the current density increased to more than 200 mA/cm² in the AENF-1/CEM configuration with Sustainion ionomer (**Figure S15a**). The FE_{CO} is only ~80% at 100 mA/cm² and decreases to less than 50% with the current density increased to more than 200 mA/cm² in the CEM-only configuration with Sustainion ionomer (**Figure S15b**). Nafion ionomer exhibits superior FE_{CO} than anion-exchange Sustainion ionomer, which should be attribute to that Nafion ionomer serves as the cation-augmenting layer which amplifying the cation effect to stabilizes key *CO₂⁻ intermediates and maintains high local pH in acidic eCO₂R. Such observation agrees well with recent report which used Nafion-K⁺ interfacial cation matrix to boost selective eCO₂R in acid.⁴⁵ In contrast, anion-exchange ionomers like Sustainion®XA-9 lack this cation-concentrating capability, leading to suboptimal interfacial ion distribution and diminished eCO₂R selectivity.

Meanwhile, cell voltage breakdown analysis was systematically conducted using the reported method,⁴⁶ where the total cell voltage of could be deconvoluted into thermodynamic potential, cathode overpotential (**Figure S16**), anode overpotential (**Figure S17**), ohmic loss (**Figure S18**), Nernstian pH loss, and other interfacial losses (**see Supplementary Note**). The breakdown of cell voltages for different MEA configurations: CEM-only (3.23 V) and AENF-1 (3.51 V) are summarized in **Figures S19** and **Figure S20**. The ohmic losses for AENF/CEM and CEM-only configuration were 0.42 ± 0.01 V and 0.16 ± 0.02 V, respectively, which including the resistance of the membrane and electrode/membrane interface.⁴⁵ The voltage loss of the AENF-1 was estimated to be 0.26 V.



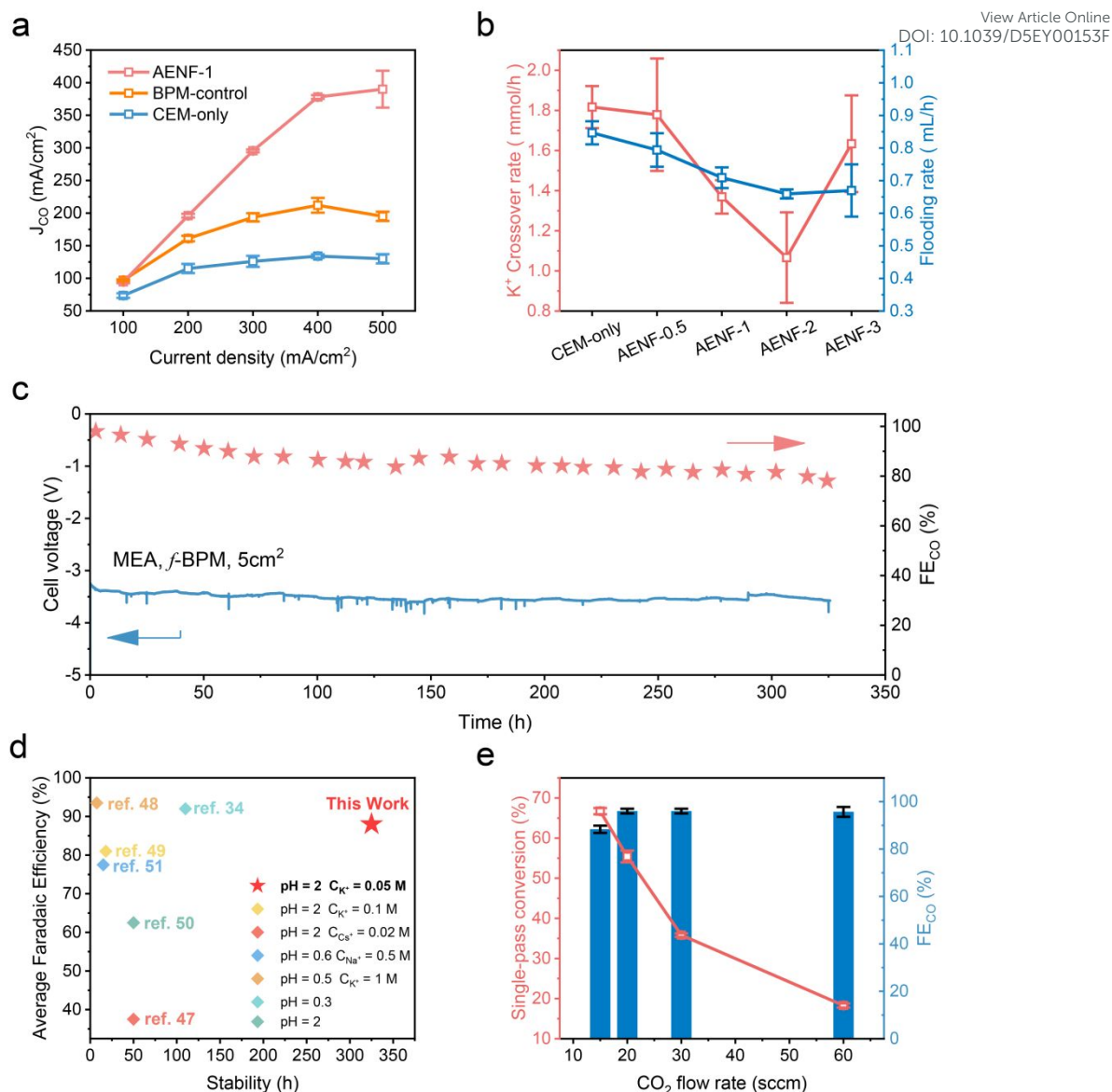


Figure 5. eCO₂R performance of AENF-1 in a 5 cm² acidic MEA setup. (a) Comparison of partial CO current densities for cases of AENF-1/Nafion-HP, BPM-Control and CEM-only. (b) Measured K⁺ crossover and flooding rates for AENF-*x* in reference to the CEM-only case. (c) Long-term stability test at 100 mA/cm² with AENF-1. (d) Comparison of the eCO₂R performance in this work with state-of-the-art literature results.^{34, 47-51} (e) Single-pass conversion of CO₂ at 300 mA/cm² under different CO₂ flow rates.

At higher current densities of 400 and 500 mA/cm², all AENF-*x* membranes exhibited increased H₂ production, accompanied by a significant rise in cell voltage. This strong correlation between H₂ yield and cell voltage underscores the detrimental impact of high cell voltages, which enhance both H⁺ and K⁺ migration. Increasing the MTCP/PVDF ratio from 0.5 to 1 reduced the full-cell voltage across all current densities, owing to the high ion conductivity of MTCP. However, further increasing the ratio to *x* = 2 and 3 did not yield substantial improvements in CO production, possibly due to the excessive membrane swelling and reduced



gas permeability, which hinder CO₂ recirculation at the bipolar interface and restrict CO₂ supply at higher current densities. AENF-1 also demonstrated the highest CO partial current density of 390 mA/cm², which is three times that of the CEM-only case and 1.8 times that of the control BPM (**Figure 4h** and **Figure 5a**). This exceptional performance highlights the optimal balance between ion conductivity and swelling achieved by AENF-1, making it the preferred choice for *f*-BPM configuration in this study. The results reveal a critical trade-off between ion conductivity and membrane swelling in modulating CO production. Additionally, the elevated cell voltage introduced by the bipolar junction partially offsets the benefits of Donnan exclusion in suppressing cation migration, adding more complexity to the system design.

To validate the reduction in K⁺ and water permeation across the electrospun nanofibers with increasing MTCP content, K⁺ crossover and water flooding rates were quantified using the previously described method (**Figure 5b**). In the absence of a bipolar junction, Nafion-HP used as the standalone CEM exhibited the highest levels of both K⁺ crossover and water flooding. As the MTCP/PVDF ratio increased from 0.5 to 2, both K⁺ crossover and water flooding were progressively suppressed. Compared to the CEM-only case, the lowest K⁺ crossover and water flooding rates, achieved at $x = 2$, were reduced by 42% and 22%, respectively. However, for AENF-3 ($x = 3$), both water flooding and K⁺ crossover rates rebounded. This reversal is likely attributed to the poor mechanical stability of the highly swollen membrane and the dominance of the potential-driven electroosmotic effect over Donnan exclusion, leading to co-ion leakage.¹⁷

The operational stability of *f*-BPMs composed of AENF- x and Nafion-HP was evaluated in acidic MEAs under a galvanostatic current of 100 mA/cm². Among the four AENF- x samples with varying MTCP/PVDF ratios, AENF-1 demonstrated the highest stability, maintaining a CO Faradaic efficiency (FE_{CO}) above 80% for over 300 hours (**Figure 5c, S21**). This result, with an average FE_{CO} of 88% during the 325-h stability test, is among the best reported so far for acidic eCO₂R in MEA targeting CO generation (**Figure 5d and Table S4**). Additionally, the AENF-1-based MEA exhibited the lowest average cell voltage of 3.51 V, significantly outperforming AENF-0.5 (3.76 V, 40.5 h), AENF-2 (3.75 V, 52 h), and AENF-3 (3.82 V, 50 h). These results highlight the improved mass transport and minimized cell voltage achieved through optimal BPM configuration, enhancing both energy efficiency and operational stability in acidic MEAs.

View Article Online
DOI: 10.1039/D5EY00153F



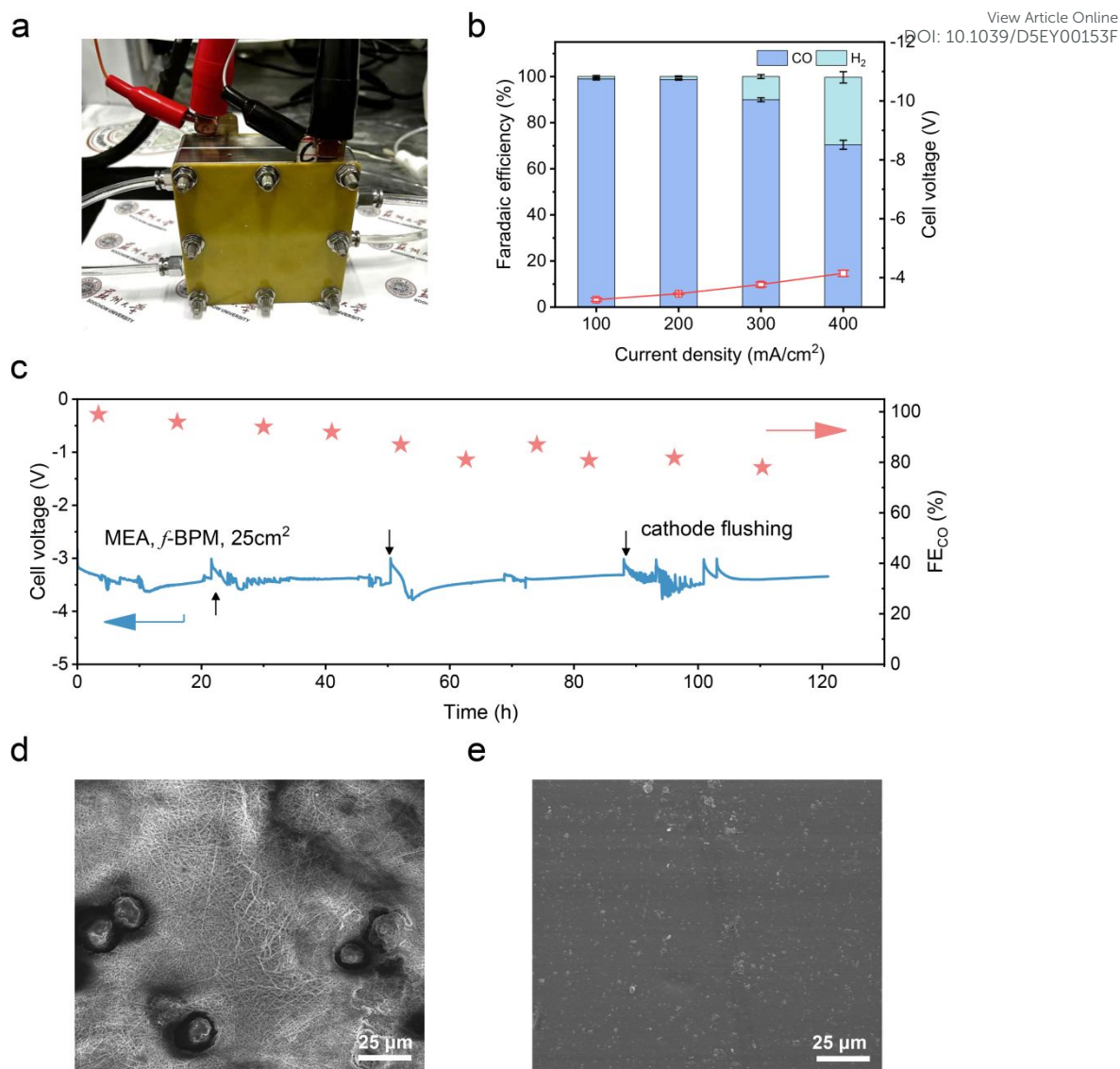


Figure 6. eCO₂R performance of a 25-cm² MEA setup employing AENF-1/Nafion-HP as the *f*-BPM under acidic condition. (a) Photograph of the MEA with a BPM form factor of 5 cm × 5 cm. (b) Faradaic efficiencies (left axis) and the corresponding cell voltages (right axis) at varying current densities. (c) Long term stability test at 100 mA/cm². (d, e) Top-view SEM images of the disassembled post-electrolytic AENF-1 and Nafion-HP membranes, respectively, for failure analysis.

CO₂ utilization efficiency is a key advantage of MEAs operating under acidic conditions. Using the most stable AENF-1 configuration, we measured the single-pass conversion (SPC) of CO₂ at 300 mA/cm² by varying the CO₂ flow rate from 15 to 60 sccm. As expected, the CO₂ conversion rate decreased with increasing flow rates, achieving a maximum SPC of 67% at 15 sccm and dropping to ~18% at 60 sccm. Notably, the total CO₂ consumption remained nearly constant across all flow rates, as quantified by multiplying the flow rate by the conversion rate. This indicates that the CO₂ conversion is primarily limited by the MEA's treatment capacity, which is approximately 10 sccm at 300 mA/cm². Under these conditions, the highest CO yield reached 9.6 mL/min (sccm), equivalent to 25.7 mmol/h.



The electrospinning method employed to fabricate AENF-*x* membranes is readily scalable, enabling the production of large-area membranes (**Figure S22**). This scalability facilitates the adoption of BPMs with larger form factors. For demonstration, we constructed a 25-cm² MEA by paring AENF-1 with Nafion-HP as shown in **Figure 6a**. The scaled-up MEA achieved near-unity CO Faradaic efficiency (FE_{CO}) at current densities of 100 and 200 mA/cm² (**Figure 6b**). Even at 300 mA/cm², with a total operating current of 7.5 A, the FE_{CO} remained above 90%. More remarkably, the MEA was able to maintain a stable operation for over 110 hours before the FE_{CO} dropped below 80%, with an average cell voltage of 3.41 V and an average FE_{CO} of 87.1% (**Figure 6c**). This performance corresponds to an impressive energy efficiency of 34.2% averaged over the entire testing period, underscoring the potential for industrial-scale deployment.

Discussion

Our MEA operations, utilizing asymmetric porous bipolar junctions of AENF-*x*/Nafion-HP and an acidic anolyte of K₂SO₄/H₂SO₄ ($C_{K^+} = 0.05\text{ M}$, pH = 2), uncovered a highly complex interplay of structural and process parameters in eCO₂R. Key factors such as film thickness, nanofiber composition, membrane swelling, mechanical strength, and full-cell voltage collectively influence product selectivity and operational stability.

1. Both K⁺ and H⁺ migration correlate with the cell voltage, which is significantly affected by the properties of AENFs at the bipolar junction. A critical trade-off exists between the application of AENFs to suppress cation migration (via Donnan exclusion) and the increased cell voltage it introduced to counteract this effect. Therefore, increasing the AENFs film thickness inhibits K⁺ crossover and HER but would be offset by the escalated cell voltage. Similarly, higher MTCP ratios in the nanofibers reduce K⁺ and H⁺ crossover but exacerbate swelling, leading to augmented electroosmosis, hindered CO₂ recirculation, and compromised mechanical stability.

2. Achieving a delicate balance among ion conductivity, membrane swelling, and mechanical strength is essential for the AENF at the bipolar junction. This balance can be finely tuned by adjusting the MTCP/PVDF ratio in the electrospun nanofibers. An optimal nanofiber structure, characterized by efficient anion transport, effective cation suppression, and moderate swelling, facilitates the recirculation of CO₂ and H₂O generated at the bipolar junction, thereby enhancing both operational stability and CO₂ utilization.

3. K⁺ crossover and water flooding are mutually reinforcing challenges in MEA operation. Severe salt precipitation from K⁺ crossover can clog gas channels in the gas diffusion electrode (GDE), impeding CO₂ mass transport and exacerbating HER. This eventually



compromises the GDE's hydrophobicity, leading to severe water flooding. On the other hand, the electroosmotic effect associated with K^+ migration draws excess water from the anolyte through the ion exchange membrane, further aggravating water flooding. To address these issues, maintaining a triphasic balance at the GDE interface is crucial. The current study achieves this balance through a bipolar junction design featuring interlaced anion-exchange nanofibers.

4. The failure mechanism of the MEAs after prolonged operation was scrutinized by carefully inspecting the disassembled device components, including the IrO_x/Ti anode, Ni-N-C cathode and AENF-1/Nafion-HP BPM. Both morphological and chemical state analyses revealed negligible changes in the cathode and anode catalysts following hundreds of hours of electrolysis (**Figure S23-S26**). Additionally, elemental analyses on the cathode effusion and anolyte via ICP-OES detected no leaching of Ni and Ir (**Table S5**), indicating that the performance decay was unlikely caused by catalyst degradation. IR spectra of AENF-1 and Nafion-HP before and after prolonged operation showed no significant changes in chemical properties (**Figure S27, S28**). However, SEM images of the disassembled *f*-BPM revealed sporadic blemished spots on the AENFs side, characterized by physically damaged and agglomerated fibers (**Figure 6d, S29**). In contrast, Nafion-HP remained intact. The blemished spots could be attributed to physical swelling and destruction of the fibrous structure caused by severe mechanical stress, inhomogeneous resistivity, and localized heating, collectively impairing the mass transport and ion-gating properties of the AENFs and ultimately leading to performance decay. Therefore, in future studies, it is necessary to further improve the durability of the AENFs to sustain harsher operational conditions at industrial scale.

Conclusion

In this work, we developed an asymmetric porous *f*-BPM architecture through the integration of electrospun AEM with two-dimensional planar CEM to address the critical challenges of CO_2 selectivity, salt precipitation, and water flooding in acidic MEA operations. The biphasic AENFs, composed of polycationic MTCP-50 and hydrophobic PVDF, were engineered to simultaneously optimize ion conductivity, membrane swelling resistance, and mechanical robustness, enabling synergistic modulation of cation migration, electrokinetic impedance, and water/gas transport properties. Through systematic optimization, AENF-1-30, featuring an optimal MTCP/PVDF ratio and moderate membrane thickness, demonstrated superior eCO_2R performance by effectively suppressing cation migration, alleviating BPM interfacial stress, and enhancing CO_2 utilization efficiency.

The acidic MEA system incorporating the optimized *f*-BPM configuration achieved remarkable stability, maintaining continuous operation for over 325 hours at 100 mA/cm^2 with



an average FE_{CO} of 88%, representing one of the highest reported values in literature. Notably, the system exhibited exceptional CO_2 utilization efficiency, achieving a high SPC of 67% at 300 mA/cm² with a CO_2 feed rate of 15 sccm. To demonstrate practical scalability, we successfully fabricated a larger 5 cm × 5 cm BPM, which maintained stable operation for 110 hours with a remarkable energy efficiency of 34.2% - the best reported so far for acidic MEA systems at this scale. These findings establish a new benchmark for acidic CO_2 electrolysis and pave the way for future investigations focusing on advanced anion-exchange chemistries and polymer matrices to enable thousand-hour stable operation under industrially relevant conditions.

View Article Online
DOI: 10.1039/D5EY00153F

Conflict of interest

The authors declare no conflict of interest.

Acknowledgments

This work is supported by the National Natural Science Foundation of China (No. 22309125, 22072101, 22075193), the Natural Science Foundation of Jiangsu Province (No. BK20220483, BK20211306, BK20220027, BK20221239), the Natural Science Foundation of the Jiangsu Higher Education Institutions of China (22KJB150010), Six Talent Peaks Project in Jiangsu Province (No. TD-XCL-006), and the Priority Academic Program Development (PAPD) of Jiangsu Higher Education Institutions.

References

1. S. Jordaan and C. Wang, *Nat. Catal.*, 2021, **4**, 915-920.
2. G. Wang, J. Chen, Y. Ding, P. Cai, L. Yi, Y. Li, C. Tu, Y. Hou, Z. Wen and L. Dai, *Chem. Soc. Rev.*, 2021, **50**, 4993-5061.
3. C. O'Brien, R. Miao, A. Zeraati, G. Lee, E. Sargent and D. Sinton, *Chem. Rev.*, 2024, **124**, 3648-3693.
4. S. Nitopi, E. Bertheussen, S. Scott, X. Liu, A. Engstfeld, S. Horch, B. Seger, I. Stephens, K. Chan, C. Hahn, J. Nørskov, T. Jaramillo and I. Chorkendorff, *Chem. Rev.*, 2019, **119**, 7610-7672.
5. H. Shin, K. Hansen and F. Jiao, *Nat. Sustain.*, 2021, **4**, 911-919.
6. R. I. Masel, Z. Liu, H. Yang, J. J. Kaczur, D. Carrillo, S. Ren, D. Salvatore and C. P. Berlinguette, *Nat. Nanotechnol.*, 2021, **16**, 118-128.
7. T. Burdyny and W. Smith, *Energy Environ. Sci.*, 2019, **12**, 1442-1453.
8. L. Ge, H. Rabiee, M. Li, S. Subramanian, Y. Zheng, J. Lee, T. Burdyny and H. Wang, *Chem*, 2022, **8**, 663-692.
9. Z. Zhang, X. Huang, Z. Chen, J. J. Zhu, B. Endrödi, C. Janáky and D. H. Deng, *Angew.*



Chem. Int. Ed, 2023, **62**, e202302789.

View Article Online
DOI: 10.1039/D5EY00153F

10. J. A. Rabinowitz and M. W. Kanan, *Nat. Commun.*, 2020, **11**, 5231.
11. T. H. Ha, J. Kim, H. Choi and J. Oh, *ACS Energy Lett.*, 2024, **9**, 4835-4842.
12. X.-F. Qiu, H.-L. Zhu, J.-R. Huang, P.-Q. Liao and X.-M. Chen, *J. Am. Chem. Soc.*, 2021, **143**, 7242-7246.
13. J. E. Huang, F. W. Li, A. Ozden, A. S. Rasouli, F. P. G. de Arquer, S. J. Liu, S. Z. Zhang, M. C. Luo, X. Wang, Y. W. Lum, Y. Xu, K. Bertens, R. K. Miao, C. T. Dinh, D. Sinton and E. H. Sargent, *Science*, 2021, **372**, 1074-1078.
14. Y. Xie, P. Ou, X. Wang, Z. Xu, Y. Li, Z. Wang, J. Huang, J. Wicks, C. McCallum, N. Wang, Y. Wang, T. Chen, B. Lo, D. Sinton, J. Yu, Y. Wang and E. Sargent, *Nat. Catal.*, 2022, **5**, 564-570.
15. Y. Zhao, L. Hao, A. Ozden, S. Liu, R. K. Miao, P. Ou, T. Alkayyali, S. Zhang, J. Ning, Y. Liang, Y. Xu, M. Fan, Y. Chen, J. E. Huang, K. Xie, J. Zhang, C. P. O'Brien, F. Li, E. H. Sargent and D. Sinton, *Nat. Synth.*, 2023, **2**, 403-412.
16. M. Zeng, W. Fang, Y. Cen, X. Zhang, Y. Hu and B. Xia, *Angew. Chem. Int. Ed*, 2024, **63**, e202404574.
17. J. C. Bui, E. W. Lees, D. H. Marin, T. N. Stovall, L. Chen, A. Kusoglu, A. C. Nielander, T. F. Jaramillo, S. W. Boettcher, A. T. Bell and A. Z. Weber, *Nat. Chem. Eng.*, 2024, **1**, 45-60.
18. M. Rashid, S. Nabil, M. Adnan, K. Kannimuthu and M. Kibria, *Adv. Energy Mater.*, 2024, **14**, 202400570.
19. Q. Bai, L. Xiong, Y. Zhang, M. Ma, Z. Jiao, F. Lyu, Z. Deng and Y. Peng, *EES Catal.*, 2024, **2**, 1228-1237.
20. T. Ha, J. Kim, H. Choi and J. Oh, *ACS Energy Lett.*, 2024, **9**, 4835-4842.
21. J. Gu, S. Liu, W. Ni, W. Ren, S. Haussener and X. Hu, *Nat. Catal.*, 2022, **5**, 268-276.
22. Z. Ma, Z. Yang, W. Lai, Q. Wang, Y. Qiao, H. Tao, C. Lian, M. Liu, C. Ma, A. Pan and H. Huang, *Nat. Commun.*, 2022, **13**, 7596.
23. B. Pan, Y. Wang and Y. Li, *Chem Catal.*, 2022, **2**, 1267-1276.
24. M. Fan, J. Huang, R. Miao, Y. Mao, P. Ou, F. Li, X. Li, Y. Cao, Z. Zhang, J. Zhang, Y. Yan, A. Ozden, W. Ni, Y. Wang, Y. Zhao, Z. Chen, B. Khatir, C. O'Brien, Y. Xu, Y. Xiao, G. Waterhouse, K. Golovin, Z. Wang, E. Sargent and D. Sinton, *Nat. Catal.*, 2023, **6**, 763-772.
25. X. She, L. Zhai, Y. Wang, P. Xiong, M. Li, T. Wu, M. Wong, X. Guo, Z. Xu, H. Li, H. Xu, Y. Zhu, S. Tsang and S. Lau, *Nat. Energy*, 2024, **9**, 154-162.
26. Y. Li, Z. Yan, J. Hitt, R. Wycisk, P. Pintauro and T. Mallouk, *Adv. Sustainable Syst.*, 2018, **2**, 1700187.
27. D. Song, Y. Lian, M. Wang, Y. Su, F. Lyu, Z. Deng and Y. Peng, *eScience*, 2023, **3**, 100097.
28. R. Fischer, M. Dessieux, F. Marone and F. Büchi, *ACS Appl. Energy Mater.*, 2024, **7**, 3590-3601.
29. J. Disch, S. Ingenhoven and S. Vierrath, *Adv. Energy Mater.*, 2023, **13**, 202400570.
30. T. Alkayyali, A. S. Zeraati, H. Mar, F. Arabyarmohammadi, S. Saber, R. K. Miao, C. P. O'Brien, H. Liu, Z. Xie, G. Wang, E. H. Sargent, N. Zhao and D. Sinton, *ACS Energy Lett.*, 2023, **8**, 4674-4683.



31. M. Hesselmann, J. Lee, S. Chae, A. Tricker, R. Keller, M. Wessling, J. Su, D. Kushner, A. Weber and X. Peng, *ACS Appl. Mater. Interfaces*, 2024, **16**, 24649-24659. View Article Online
DOI: 10.1039/D5EY00153F
32. Y. Xu, R. Miao, J. Edwards, S. Liu, C. O'Brien, C. Gabardo, M. Fan, J. Huang, A. Robb, E. Sargent and D. Sinton, *Joule*, 2022, **6**, 1333-1343.
33. W. Song, K. Peng, W. Xu, X. Liu, H. Zhang, X. Liang, B. Ye, H. Zhang, Z. Yang, L. Wu, X. Ge and T. Xu, *Nat. Commun.*, 2023, **14**, 2732.
34. B. Wu, B. Wang, B. Cai, C. Wu, W. W. Tjiu, M. Zhang, Z. Aabdin, S. Xi and Y. Lum, *J. Am. Chem. Soc.*, 2024, **146**, 29801-29809.
35. S. Hao, A. Elgazzar, N. Ravi, T.-U. Wi, P. Zhu, Y. Feng, Y. Xia, F.-Y. Chen, X. Shan and H. Wang, *Nat. Energy*, 2025, **10**, 266-277.
36. W. Hua, H. Sun, L. Lin, Q. Mu, B. Yang, Y. Su, H. Wu, F. Lyu, J. Zhong, Z. Deng and Y. Peng, *Chem. Eng. J.*, 2022, **446**, 137296.
37. H. Wang, X. Wu, G. Liu, S. Wu and R. Xu, *Nano Res.*, 2023, **16**, 4546-4553.
38. P. Su, K. Iwase, S. Nakanishi, K. Hashimoto and K. Kamiya, *Small*, 2016, **12**, 6083-6089.
39. C. Lv, K. Huang, H. Xu, G. Sun, H. Zheng, C. Lian, Y. Zhang, C. Ma, J. Wang and L. Ling, *ACS Sustainable Chem. Eng.*, 2024, **12**, 11901-11912.
40. S. Kato, S. Ito, S. Nakahata, R. Kurihara, T. Harada, S. Nakanishi and K. Kamiya, *ChemSusChem*, 2024, **17**, e202401013.
41. J. Biemolt, J. Singh, G. Prats Vergel, H. M. Pelzer and T. Burdyny, *ACS Energy Lett.*, 2025, **10**, 807-814.
42. N. Chen and Y. Lee, *Trends Chem.*, 2022, **4**, 236-249.
43. S. Garg, C. Rodriguez, T. Rufford, J. Varcoe and B. Seger, *Energy Environ. Sci.*, 2022, **15**, 4440-4469.
44. S. Favero, I. Stephens and M. Titirci, *Adv. Mater.*, 2024, **36**, 2308238.
45. A. Shayesteh Zeraati, F. Li, T. Alkayyali, R. Dorakhan, E. Shirzadi, F. Arabyarmohammadi, C. P. O'Brien, C. M. Gabardo, J. Kong, A. Ozden, M. Zargartalebi, Y. Zhao, L. Fan, P. Papangelakis, D. Kim, S. Park, R. K. Miao, J. P. Edwards, D. Young, A. H. Ip, E. H. Sargent and D. Sinton, *Nat. Synth.*, 2025, **4**, 75-83.
46. K. Xie, R. K. Miao, A. Ozden, S. J. Liu, Z. Chen, C. T. Dinh, J. E. Huang, Q. C. Xu, C. M. Gabardo, G. Lee, J. P. Edwards, C. P. O'Brien, S. W. Boettcher, D. Sinton and E. H. Sargent, *Nat. Commun.*, 2022, **13**, 3609.
47. B. Pan, J. Fan, J. Zhang, Y. Luo, C. Shen, C. Wang, Y. Wang and Y. Li, *ACS Energy Lett.*, 2022, **7**, 4224-4231.
48. H. Li, H. Li, P. Wei, Y. Wang, Y. Zang, D. Gao, G. Wang and X. Bao, *Energy Environ. Sci.*, 2023, **16**, 1502-1510.
49. M. Wang, L. Lin, Z. Y. Zheng, Z. Y. Jiao, W. Hua, G. W. Wang, X. X. Ke, Y. B. Lian, F. Lyu, J. Zhong, Z. Deng and Y. Peng, *Energy Environ. Sci.*, 2023, **16**, 4423-4431.
50. J. Fan, B. Pan, J. Wu, C. Shao, Z. Wen, Y. Yan, Y. Wang and Y. Li, *Angew. Chem. Int. Ed.*, 2024, **63**, e202317828.
51. Z. Liu, T. Yan, H. Shi, H. Pan, Y. Cheng and P. Kang, *ACS Appl. Mater. Interfaces*, 2022, **14**, 7900-7908.



Data availability statement

View Article Online
DOI: 10.1039/D5EY00153F

Further information and requests for resources should be directed to and will be fulfilled by the corresponding author.

